Atmos. Chem. Phys., 24, 3989–4000, 2024
https://doi.org/10.5194/acp-24-3989-2024

Atmospheric Chemistry and Physics
Open Access
EGU

Molecular-level study on the role of methanesulfonic acid in iodine oxoacid nucleation

Jing Li[1], Nan Wu[1], Biwu Chu[2,3], An Ning[1], and Xiuhui Zhang[1]

[1]Key Laboratory of Cluster Science, Ministry of Education of China, School of Chemistry and Chemical Engineering, Beijing Institute of Technology, Beijing, 100081, China
[2]State Key Joint Laboratory of Environment Simulation and Pollution Control, Research Center for Eco-Environmental Sciences, Chinese Academy of Sciences, Beijing, 100085, China
[3]College of Resources and Environment, University of Chinese Academy of Sciences, Beijing, 100049, China

Correspondence: An Ning (anning@bit.edu.cn) and Xiuhui Zhang (zhangxiuhui@bit.edu.cn)

Received: 11 September 2023 – Discussion started: 11 October 2023
Revised: 12 February 2024 – Accepted: 15 February 2024 – Published: 3 April 2024

Abstract. Iodic acid (HIO_3) and iodous acid (HIO_2) have been identified as nucleating effectively by the Cosmics Leaving Outdoor Droplets (CLOUD) experiment at CERN, yet it may be hard to explain all HIO_3-induced nucleation. Given the complexity of marine atmosphere, other precursors may be involved. Methanesulfonic acid (MSA), as a widespread precursor over oceans, has been proven to play a vital role in facilitating nucleation. However, its kinetic impacts on the synergistic nucleation of iodine oxoacids remain unclear. Hence, we investigated the MSA-involved HIO_3–HIO_2 nucleation process at the molecular level using density functional theory (DFT) and the Atmospheric Cluster Dynamics Code (ACDC). Our results show that MSA can form stable molecular clusters with HIO_3 and HIO_2 jointed via hydrogen bonds, halogen bonds, and electrostatic attraction after proton transfer to HIO_2. Thermodynamically, the MSA-involved clustering can occur nearly without a free-energy barrier, following the HIO_2–MSA binary and HIO_3–HIO_2–MSA ternary pathway. Furthermore, our results show that considering MSA will significantly enhance the calculated rate of HIO_3–HIO_2-based cluster formation, by up to 10^4-fold in cold marine regions containing rich MSA and scarce iodine, such as the polar regions Ny-Ålesund and Marambio. Thus, the proposed more efficient HIO_3–HIO_2–MSA nucleation mechanism may provide theoretical evidence for explaining the frequent and intensive bursts of marine iodine particles.

1 Introduction

Marine aerosol, which is the primary natural aerosol (O'Dowd and de Leeuw, 2007), has a significant impact on global climate, radiation balance, and even human health (Wang et al., 2010; Pöschl, 2005). New particle formation (NPF) is a primary source of marine aerosols, which proceeds via nucleation and subsequent growth (Lee et al., 2019; Zhang, 2010; Kulmala et al., 2013; Zhang et al., 2012). Moreover, nucleation, forming critical clusters at 1–2 nm from gaseous precursors, is the pivotal step affecting NPF (Zhang, 2010; Kulmala et al., 2013). However, the chemicals involved in nucleation and the underlying mechanisms remain poorly understood due to technological limitations in molecular-level analysis. Additionally, a lack of comprehensive and long-term ocean observations further hinders our knowledge of marine NPF.

Recent field studies have suggested that marine NPF events are closely related to atmospheric iodine-bearing molecules emitted by algae (Yu et al., 2019; Baccarini et al., 2020; Beck et al., 2021). During NPF events in coastal areas (e.g., Mace Head and Zhejiang; Sipilä et al., 2016; Yu et al., 2019) and polar oceans (e.g., Arctic Ocean) (Baccarini et al., 2020), the nucleation processes are mainly driven by iodic acids (HIO_3). However, the self-nucleation of HIO_3 alone cannot fully explain the observed NPF rates (Rong et al., 2020). More recently, the Cosmics Leaving Outdoor Droplets (CLOUD) experiment at CERN has found that iodous acid (HIO_2) plays a key role in stabilizing HIO_3,

enabling effective nucleation by the sequential addition of HIO_3 followed by HIO_2 (He et al., 2021). Further theoretical studies have uncovered the fact that the stabilizing effect of HIO_2 on HIO_3 stems from its role as a base in clustering (S. Zhang et al., 2022; Liu et al., 2023). Although the efficient nucleation of HIO_3 and HIO_2 is overall consistent with the CLOUD measurement (R. Zhang et al., 2022), this mechanism does not account for all HIO_3-induced nucleation in the authentic atmosphere (Ma et al., 2023). Thus, other essential precursors in the marine atmosphere might potentially affect HIO_3–HIO_2 nucleation, but which ones have an effect and how remain largely unexamined.

Methanesulfonic acid (MSA), as a typical marine sulfur precursor, is widespread over oceans (Saltzman et al., 1983; Read et al., 2008; Chen et al., 2012; Yan et al., 2019) with considerable atmospheric concentrations (10^5–10^8 molec. cm^{-3}) (Eisele and Tanner, 1993; Dal Maso et al., 2002; Chen et al., 2018; Yan et al., 2019). Moreover, MSA has been shown to initiate nucleation with vital atmospheric precursors, such as ammonia and amines, enhancing cluster formation (O'Dowd et al., 2002; Bork et al., 2014; Shen et al., 2019, 2020; Brean et al., 2021; Liu et al., 2022). Importantly, current evidence suggests that MSA can also form stable clusters with HIO_3 or HIO_2 individually, but none of the resulting binary nucleation can explain field measurements well (Ning et al., 2022; Wu et al., 2023). Despite the stabilizing effect of MSA on iodine oxoacids, whether MSA can synergistically nucleate with HIO_3 and HIO_2, as well as the induced kinetic impacts on clustering, remains unknown. Furthermore, given the coexistence of MSA and HIO_3 in different marine regions (Quéléver et al., 2022; Beck et al., 2021), along with the consistent presence of HIO_3 and HIO_2 as homologous substances (Sipilä et al., 2016), the importance of the HIO_3–HIO_2–MSA nucleation mechanism may differ under distinct ambient conditions, but this remains unclear.

Herein, we have systematically investigated the HIO_3–HIO_2-based nucleation involved in MSA, including $(HIO_3)_x(HIO_2)_y(MSA)_z$ $(1 \le x+y+z \le 5,\ 0 \le z \le 3)$ clusters, by combining a quantum chemical (QC) approach with the Atmospheric Cluster Dynamics Code (ACDC) (McGrath et al., 2012). To probe the nature of cluster formation and investigate the intermolecular interactions, wave-function analysis was performed. Additionally, the Gibbs free energies of cluster formation were calculated to evaluate cluster stability. Moreover, a series of ACDC simulations were executed to delve into the influence of MSA on nucleation rates and mechanisms under varying atmospheric conditions, such as regarding precursor concentration and temperature.

2 Methods

2.1 Quantum chemistry calculations

To locate the low-lying isomers of $(HIO_3)_x(HIO_2)_y(MSA)_z$ $(1 \le x+y+z \le 5,\ 0 \le z \le 3)$ clusters, the multi-step conformer search was adopted here (details in the Supplement). The resulting stable clusters with the lowest energies were identified at the ωB97X-D/6-311++G(3df,3pd) (for C, H, O, and S atoms) + aug-cc-pVTZ-PP with ECP28MDF (for the I atom) level of theory (Francl et al., 1982; Peterson et al., 2003), and the corresponding Cartesian coordinates are collected in Table S9 in the Supplement. In addition, the structures of pure HIO_3, pure HIO_2, pure MSA, HIO_3–HIO_2, HIO_3–MSA, and HIO_2–MSA clusters in the present study have been adopted from previous studies (Rong et al., 2020; S. Zhang et al., 2022; Liu et al., 2023; Ning et al., 2022; Wu et al., 2023). All density functional theory (DFT) calculations were carried out using the Gaussian 09 package (Frisch et al., 2009), where FineGrid and tight convergence were employed. The single-point energy was calculated at the RI-CC2/aug-cc-pVTZ (for C, H, and O atoms) + aug-cc-pV(T+d)Z (for the S atom) + aug-cc-pVTZ-PP with ECP28MDF (for the I atom) level of theory (Hättig and Weigend, 2000) by the TURBOMOLE program (Ahlrichs et al., 1989) because of its success in fitting with the experiments (Lu et al., 2020; Kürten et al., 2018; Rong et al., 2020; Almeida et al., 2013). In the present study, the Gibbs formation free energy (ΔG_{ref}, kcal mol^{-1}) of the HIO_3–HIO_2–MSA clusters at the reference pressure (1 atm) was calculated as

$$\Delta \mathrm{G_{ref}} = \Delta E_{\mathrm{RI-CC2}} + \Delta G^{\omega \mathrm{B97X-D}}_{\mathrm{thermal}}, \quad (1)$$

where $\Delta E_{\mathrm{RI-CC2}}$ is the electronic contribution and $\Delta \mathrm{G}^{\omega \mathrm{B97X-D}}_{\mathrm{thermal}}$ is the thermal contribution to free energy. The ΔG_{ref} values at different temperatures ($T = 258$–298 K) were calculated using the Shermo 2.0 code (Lu and Chen, 2021) and are collected in Table S1. Further, given the effect of the precursor's vapor pressures, the ΔG_{ref} was converted into $\Delta G(P_1, P_2, \ldots, P_n)$ (Vehkamäki, 2006) by Eq. (2):

$$\Delta G(P_1, P_2, \ldots, P_n) = \Delta G_{\mathrm{ref}} - k_{\mathrm{B}} T \sum_{i=1}^{n} N_i \ln\left(\frac{P_i}{P_{\mathrm{ref}}}\right), \quad (2)$$

where n is the number of components within the cluster, k_{B} denotes the Boltzmann constant, T signifies the temperature, N_i refers to the number of molecules of type i in the number of components in the cluster, and P_i is the partial pressure of component i in the vapor phase.

2.2 Wave-function analysis

Wave-function analysis was carried out using Multiwfn 3.7 (Lu and Chen, 2012) to investigate the binding nature within molecular clusters. The electrostatic potential (ESP) on the

van der Waals (vdW) surface was calculated to identify active interaction sites. Specifically, the negative ESP region is electron-rich, while the positive ESP region is electron-deficient, potentially leading to mutual non-covalent interactions, such as hydrogen bonds (HBs) and halogen bonds (XBs). To further quantify the bond strength, the electron density $\rho(r)$, Laplacian electron density $\nabla^2\rho(r)$, and energy density $H(r)$ at bond critical points (BCPs) were calculated based on the atoms-in-molecules (AIM) theory (Lane et al., 2013).

2.3 Atmospheric cluster dynamic simulations

To explore nucleation kinetics, the Atmospheric Cluster Dynamics Code (ACDC) (McGrath et al., 2012) was adopted here to compute the cluster formation rates, steady-state concentrations, and formation pathways by explicit solution of the birth–death equations (Eq. 3).

$$\frac{\mathrm{d}C_i}{\mathrm{d}t} = \frac{1}{2}\sum_{j<i}\beta_{j,(i-j)}C_jC_{(i-j)} + \sum_j \gamma_{(i+j)\to i}C_{i+j} - \sum_j \beta_{i,j}C_iC_j - \frac{1}{2}\sum_{j<i}\gamma_{i\to j}C_i + Q_i - S_i\,, \quad (3)$$

where the subscripts i, j, $i-j$, and $i+j$ denote different clusters or monomers; C_i is the concentration of cluster i; and $\beta_{i,j}$ and $\gamma_{(i+j)\to i}$ represent the cluster collision and evaporation rate coefficient, respectively. Q_i and S_i denote the external source and sink terms, respectively. $\beta_{i,j}$ is calculated as follows:

$$\beta_{i,j} = \left(\frac{3}{4\pi}\right)^{1/6}\left(\frac{6k_\mathrm{B}T}{m_i}+\frac{6k_\mathrm{B}T}{m_j}\right)^{1/2}\left(V_i^{1/3}+V_j^{1/3}\right)^2, \quad (4)$$

where m_i and V_i represent the mass and volume of cluster i, respectively. $V_i = 3/4\times\pi\times(d_i/2)^3$, where the diameter d_i of cluster i is derived from the cluster volume V_i calculated by Multiwfn 3.7 (Lu and Chen, 2012). $\gamma_{(i+j)\to i}$ is calculated by Eq. (5):

$$\gamma_{(i+j)\to i} = \beta_{i,j}\frac{P_\mathrm{ref}}{k_\mathrm{B}T}\exp\left(\frac{\Delta G_{i+j}-\Delta G_i-\Delta G_j}{k_\mathrm{B}T}\right), \quad (5)$$

where P_ref is the reference pressure at 1 atm and ΔG is the formation free energy of the cluster.

In the ACDC simulations performed, we considered all possible collision and evaporation processes, including monomer–monomer, monomer–cluster, and cluster–cluster collisions, as well as decomposition of parent clusters into monomers and clusters or into two smaller clusters. Additionally, whether the clusters in the simulated system are stable depends on whether the rate of collision frequencies exceeds the total evaporation rate coefficients ($\beta C/\Sigma\gamma > 1$) (Table S4). The setting of the boundary conditions of ACDC simulations is summarized in Table S3. An uncertainty analysis was performed in this study (Table S8 and Figs. S15, S16, and S17), with details provided in the Supplement.

3 Results and discussion

Here, conformational analysis was first carried out to study how MSA affects intermolecular interactions in the HIO_3–HIO_2–MSA clusters. The thermodynamic analysis was employed to assess stability of the formed clusters. To gain insights into nucleation mechanisms, a series of ACDC simulations were executed under varying atmospheric conditions.

3.1 Cluster conformational analysis

Strong interactions among nucleation precursors are pivotal for forming stable clusters. To evaluate the binding potential of MSA with HIO_3 and HIO_2, we calculated the ESP-mapped molecular vdW surface to identify interaction sites. As illustrated in Fig. 1, MSA has a positive ESP maximum ($+63.95\,\mathrm{kcal\,mol^{-1}}$) at the H atom of its −OH group, serving as an HB donor. The iodine atoms of HIO_3 and HIO_2 with positive ESP maximums ($+51.90$ and $+45.26\,\mathrm{kcal\,mol^{-1}}$) can act as XB donors. Additionally, the oxygen atoms in the S=O group (from MSA) and I=O group (from HIO_3 and HIO_2) with strong electronegativity can act as HB or XB acceptor sites due to the lone-pair electrons. Therefore, as shown in Fig. 1d, MSA, HIO_3, and HIO_2 have the potential to form clusters via intermolecular HBs and XBs.

As presented in Fig. 2, all the identified HIO_3–HIO_2–MSA clusters are structurally stabilized by the network of HBs (dashed blue lines) and XBs (dashed red lines). Within these clusters, the inward-facing oxygen atom and hydroxyl (−OH) group in MSA facilitates it being involved in forming more HBs and XBs compared to the HIO_3–HIO_2 clusters (Fig. S1 in the Supplement). Statistically, within HIO_3–HIO_2–MSA clusters, the percentage of XBs (61 %) is higher than that of HBs (39 %). Notably, during the HIO_3–HIO_2–MSA cluster formation, HIO_2 behaves like a base and is protonated by MSA instead of HIO_3, likely due to stronger acidity of MSA than HIO_3. After the MSA-driven proton transfer to HIO_2, the resulting electrostatic interactions between the formed ion pairs ($CH_3SO_3^-$–$H_2IO_2^+$) further stabilize the clusters. Taken together, MSA can form clusters with HIO_3 and HIO_2 via HBs, XBs, and electrostatic attraction between ion pairs after proton transfer. Additionally, taking the $(HIO_3)_1(HIO_2)_3(MSA)_1$ cluster for example, there are still some potential remaining unoccupied binding sites as shown in Fig. S2. This suggests that the large-size clusters studied still have unoccupied HB and XB sites that can potentially facilitate the condensation of precursors in the atmosphere, enhancing further growth of marine aerosols.

To further quantify bond strength within HIO_3–HIO_2–MSA clusters, topological analysis was performed based on the atoms-in-molecules (AIM) theory. The electron density $\rho(r)$, Laplacian electron density $\nabla^2\rho(r)$, and energy density $H(r)$ at the corresponding bond critical points (BCPs) in the studied HIO_3–HIO_2–MSA clusters were calculated and are collected in Table S2. $\rho(r)$ is generally positively as-

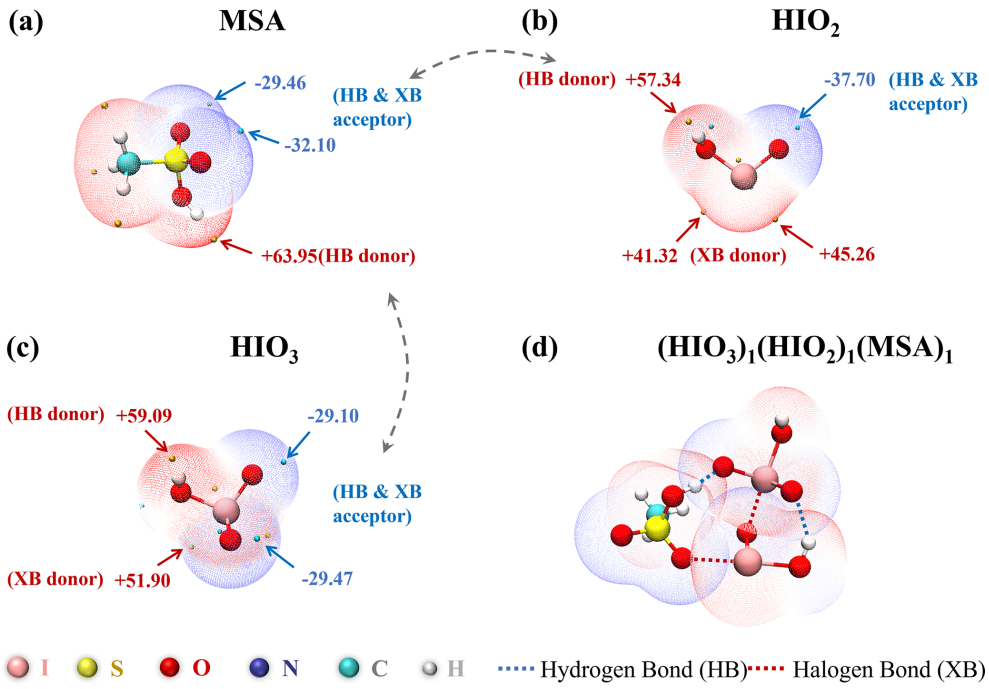

Figure 1. The ESP-mapped molecular vdW surface of **(a)** MSA, **(b)** HIO_2, **(c)** HIO_3, and **(d)** $(HIO_3)_1(HIO_2)_1(MSA)_1$. The golden and cyan dots represent the positions of maximums and minimums of ESP (units: kcal mol^{-1}), respectively. The dashed gray arrows signify the site-to-site interaction tendencies.

sociated with the bond strength. For the HIO_3–HIO_2–MSA clusters, $\rho(r)$ values at the BCPs of the HBs range from 0.0090 to 0.0869 a.u. (atomic units), exceeding the reported threshold of HB (0.002–0.040 a.u.) (Koch and Popelier, 1995; Grabowski, 2004). Moreover, the associated values of $\nabla^2\rho(r)$ at these BCPs range from 0.0310 to 0.1180 a.u., falling within the suggested range for HB (0.014–0.139 a.u.) (Koch and Popelier, 1995; Grabowski, 2004). Meanwhile, for O–I···O XBs, the $\rho(r)$ and $\nabla^2\rho(r)$ values within HIO_3–HIO_2–MSA clusters range from 0.0068 to 0.1999 and 0.0288 to 0.1744 a.u., respectively. Collectively, MSA can stabilize HIO_3–HIO_2 clusters via more relatively strong HBs and XBs while also protonating HIO_2 to form ion pairs.

3.2 Cluster formation pathways and free-energy surface

To explore how MSA affects HIO_3–HIO_2-based nucleation kinetics, the ACDC simulations were employed to reveal the nucleation mechanism under varying atmospheric conditions. Based on field measurements (Berresheim et al., 2002; Chen et al., 2018; Sipilä et al., 2016; Beck et al., 2021), the ranges of [MSA], [HIO_3], and [HIO_2] are set to be 10^6–10^8, 10^6–10^8, and 2.0×10^4–2.0×10^6 molec. cm^{-3}, respectively, where [HIO_3]/[HIO_2] is a constant. Here, the condensation sink (CS) coefficient is set to be 2.0×10^{-3} s^{-1} (Dal Maso et al., 2002) and the temperature (T) is 278 K. Under such conditions, the molecular-level nucleation pathways and the corresponding branching ratios are depicted in Fig. 3a. The detailed branch ratio is also shown at 278 K (Fig. S3) and 268 K (Fig. S4). Furthermore, to comprehend how the growth occurs thermodynamically, we herein calculated the Gibbs free energies (ΔG, Eq. 2) along the main clustering pathway at the conditions of T = 268–278 K, [HIO_3] = 1.0×10^6, [HIO_2] = 2.0×10^4, and [MSA] = 5.0×10^6 molec. cm^{-3} (Figs. 3b and S5).

As shown in Fig. 3a, the clustering pathways, at T = 278 K, CS = 2.0×10^{-3} s^{-1}, [HIO_3] = 1.0×10^6, [HIO_3] = 2.0×10^4, and [MSA] = 5.0×10^6 molec. cm^{-3}, can be categorized into two main types: (i) MSA-involved pathways, including HIO_2–MSA and HIO_3–HIO_2–MSA nucleation, and (ii) non-MSA pathways, primarily involving HIO_3–HIO_2 nucleation. For the HIO_2–MSA pathway, the initial formation of $(HIO_2)_1(MSA)_1$ heterodimers occurs without any energy barrier (Fig. 3b). The subsequent cluster growth mainly proceeds via sequential addition of HIO_2 or MSA monomers, partly coupled with cluster collisions. Specifically, 63 % of $(HIO_2)_2(MSA)_2$ results from $(HIO_2)_2(MSA)_1$ colliding with MSA monomers with an energy barrier of 1.00 kcal mol^{-1}, while 36 % results from a barrierless combination of two $(HIO_2)_1(MSA)_1$ clusters. At this point, kinetics drives growth by colliding $(HIO_2)_2(MSA)_1$ with MSA monomers, instead of following the lowest-energy pathway. This is because the collision frequency of $(HIO_2)_1(MSA)_1$ and a HIO_2 monomer is higher, stemming from the higher [HIO_2]. Then, the formed $(HIO_2)_2(MSA)_2$ further collides with a HIO_2 monomer,

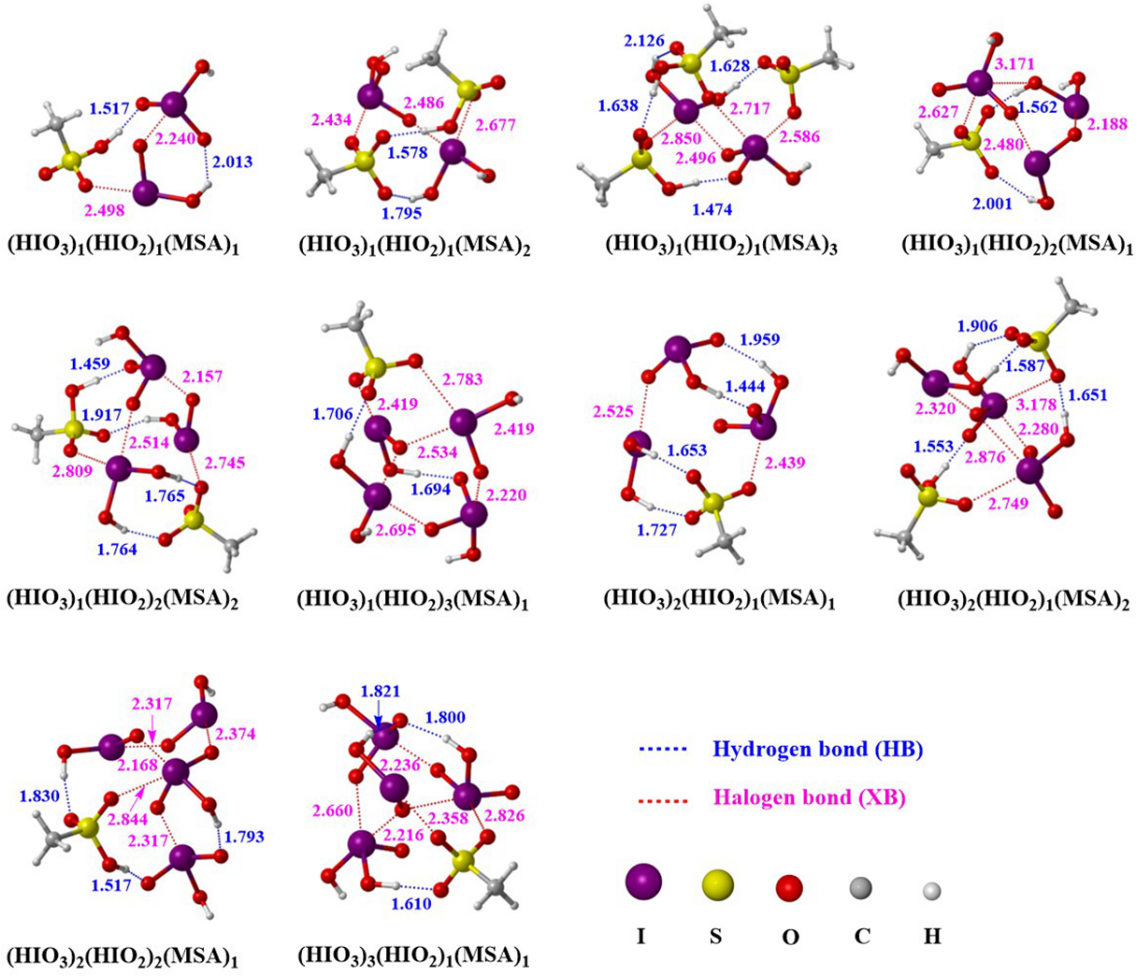

Figure 2. The most stable configurations of the HIO_3–HIO_2–MSA ternary clusters identified at the ωB97XD/6-311++G(3df, 3pd) (for C, H, O, and S atoms) + aug-cc-pVTZ-PP with ECP28MDF (for I atom) level of theory. The lengths of bonds are given in ångströms (Å).

yielding the stable $(HIO_2)_3(MSA)_2$ cluster against evaporation. As for HIO_3–HIO_2–MSA nucleation, the formation of an $(HIO_3)_1(HIO_2)_3(MSA)_1$ cluster arises from the collision of (i) $(HIO_2)_2(MSA)_1$ with $(HIO_3)_1(HIO_2)_1$ (18 %, energy barrier: 1.00 kcal mol^{-1}) and (ii) $(HIO_3)_1(HIO_2)_2$ with $(HIO_2)_1(MSA)_1$ (62 %, energy barrier: 0.17 kcal mol^{-1}), as well as (iii) $(HIO_3)_1(HIO_2)_3$ binding with a MSA monomer (20 %, energy barrier: 3.80 kcal mol^{-1}). In addition, for the non-MSA pathway marked by purple arrows, 76 % of $(HIO_3)_2(HIO_2)_2$ cluster formation arises from the collision between two $(HIO_3)_1(HIO_2)_1$ clusters, which accords closely with the barrierless pathway shown in Fig. 3b.

Overall, the MSA-involved pathways contribute to 74 % of cluster formation, while the non-MSA path accounts for only 26 %. Although the HIO_3–HIO_2–MSA growth pathway is less favorable than the HIO_3–HIO_2 and HIO_2–MSA pathways at $T = 278$ K, it can become barrierless at a lower temperature of 268 K (Fig. S5). This result may be explained by the fact that the lower temperature results in a decrease in the evaporation rates of the HIO_3–HIO_2–MSA clusters. The detailed cluster evaporation paths and corresponding γ at 268 and 278 K are collected in Tables S5 and S6. Generally, stable clusters have lower evaporation rates. According to the calculated cluster evaporation rates ($\Sigma\gamma$, s^{-1}) at 278 K (Table S7), more than 40 % of the clusters have $\Sigma\gamma$ values less than 10^{-3} s^{-1}, indicating relatively high stability ($\beta C/\Sigma\gamma > 1$). Among these resulting stable clusters (see Fig. S6), the majority (85 %) contain HIO_2. Moreover, the concentration of these stable clusters increases gradually with time, even reaching a maximum of 10^4 molec. cm^{-3} (Fig. S6). Of these stable clusters, initial $(HIO_3)_1(HIO_2)_1$, $(HIO_2)_2$, and $(MSA)_1(HIO_2)_1$ dimers form rapidly, and at $t \approx 1$ s, heterotrimers $(HIO_3)_1(HIO_2)_2$ and $(MSA)_1(HIO_2)_2$ begin to form, after which the larger-sized clusters also form. This time-dependent evidence suggests that MSA is involved in the whole clustering process, from the initial formation of smaller clusters to the large-sized nucleated clusters that potentially further grow. Taken together, these findings high-

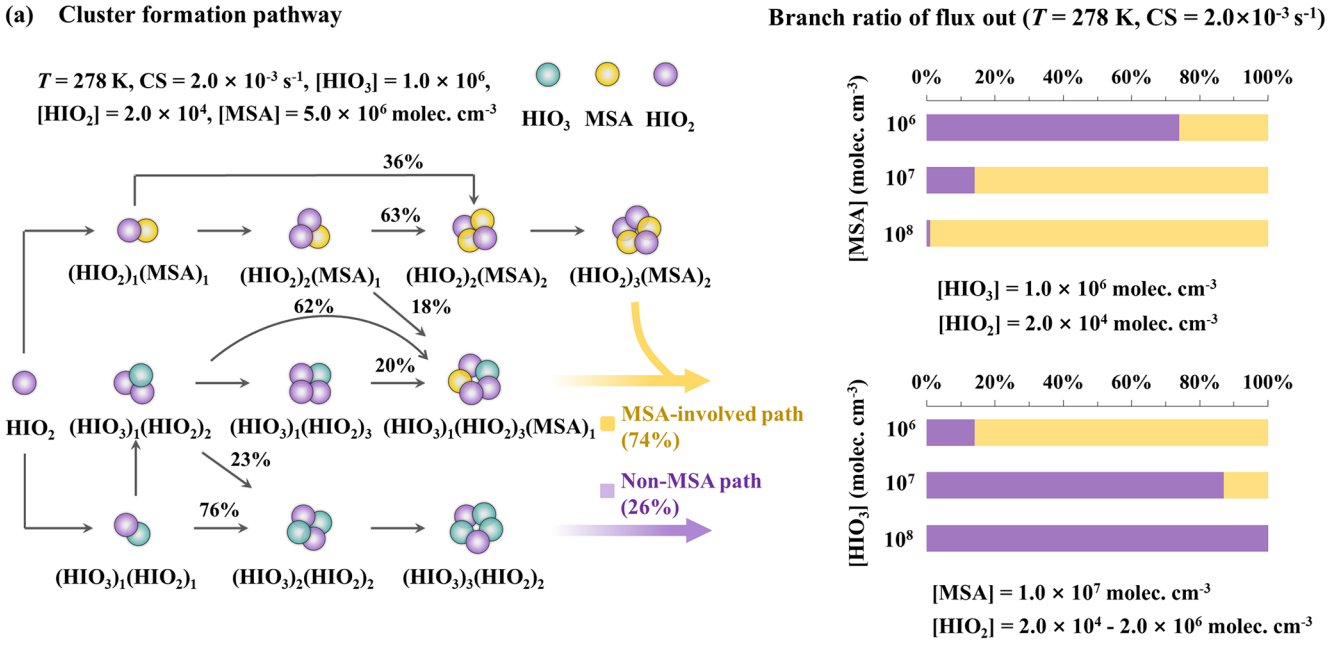

(b) Free energy surface of cluster formation

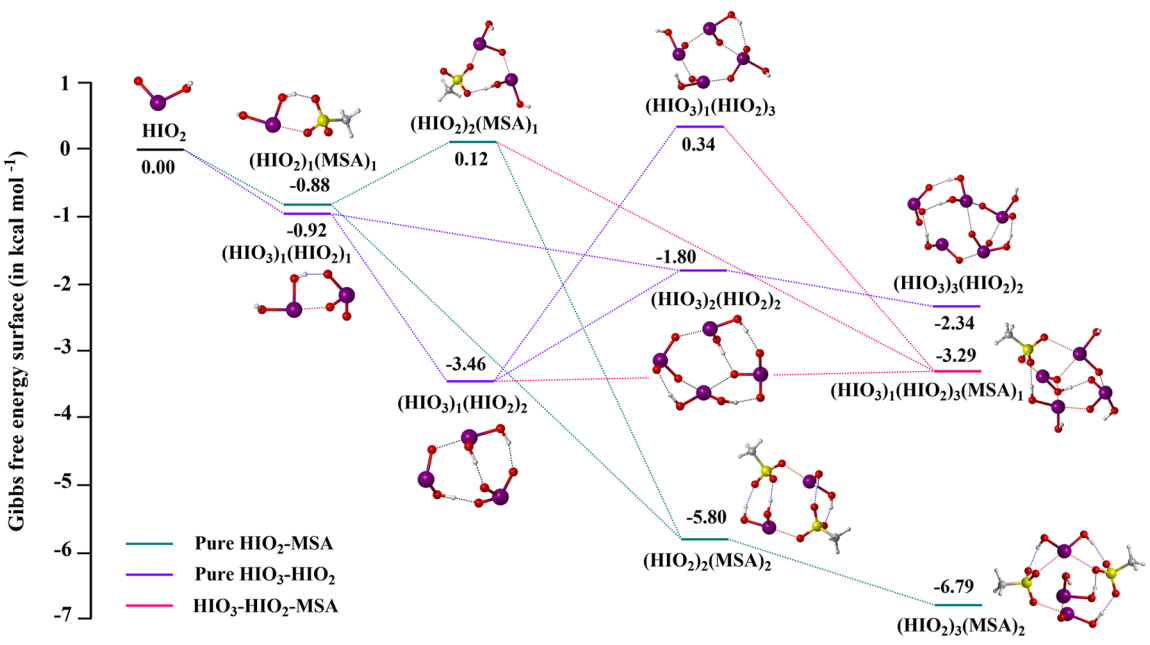

Figure 3. **(a)** Left: the main cluster growth pathway of the HIO_3–HIO_2–MSA nucleation system at $T = 278$ K, CS $= 2.0 \times 10^{-3}$ s^{-1}, $[HIO_3] = 1.0 \times 10^6$, $[HIO_2] = 2.0 \times 10^4$, and $[MSA] = 5.0 \times 10^6$ molec. cm^{-3}. Right: the branch ratio of outward flux under varying [MSA] (10^6–10^8 molec. cm^{-3}) and $[HIO_3]$ (10^6–10^8 molec. cm^{-3}) values. The yellow and purple arrows (or bars) denote MSA-involved and non-MSA outward flux (or branch ratio), respectively. **(b)** The Gibbs free energies of cluster formation (ΔG, kcal mol^{-1}) based on the main clustering pathway in the HIO_3–HIO_2–MSA nucleation system. $[HIO_3]/[HIO_2]$ is a constant.

light the direct and significant involvement of MSA in HIO_3–HIO_2 nucleation, facilitating cluster formation.

As presented on the right of Fig. 3a, the contribution of different clustering pathways to the outward flux varies with precursor concentrations. With increasing [MSA] from 10^6 to 10^8 molec. cm^{-3}, the contribution of MSA-involved pathways rises from 1 % to 99 % during nucleation. At the median [MSA] of 10^7 molec. cm^{-3}, the MSA-involved pathway contributes 86 %, whereas the non-MSA pathway accounts for just 14 %. In contrast, the ratio of MSA-involved pathways decreases (from 86 % to 0 %) with increasing concentrations of iodine oxoacids. At higher [HIO_3] values of 10^8 molec. cm^{-3}, the HIO_3–HIO_2 pathway dominates nucleation. Predictably, the kinetic impact of MSA on HIO_3–HIO_2 nucleation is more pronounced in marine regions with richer MSA away from iodine sources.

3.3 Enhancement of cluster formation rates

Guided by the clustering pathway analysis, MSA has shown its potential to participate in the HIO_3–HIO_2-based nucleation, but its detailed impacts on cluster formation rates (J, $cm^{-3}\ s^{-1}$) remain uncertain. The influence of MSA on J under different atmospheric conditions is systematically analyzed below.

Figure 4 presents the simulated J of the HIO_3–HIO_2–MSA (red bar) and HIO_3–HIO_2 system (gray bar) against the varying temperatures (T = 258–298 K) at CS = $2.0\times10^{-3}\ s^{-1}$, [HIO_3] = 1.0×10^7, [HIO_2] = 2.0×10^5, and [MSA] = 1.0×10^7 molec. cm^{-3}. Clearly, J(HIO_3–HIO_2–MSA) is consistently higher than J(HIO_3–HIO_2), highlighting the enhancement effect of MSA on HIO_3–HIO_2-based clustering under common atmospheric temperatures. Specifically, both J(HIO_3–HIO_2–MSA) and J(HIO_3–HIO_2) are negatively dependent on T due to reduced cluster evaporation caused by low T. As a result, MSA could promote nucleation with higher J, especially in the colder regions, such as polar oceans.

It is worth noting that apart from atmospheric temperature, precursor concentrations might also vary regionally or seasonally, which can further affect nucleation. So, to comprehensively reveal the effect of MSA, here we defined and calculated MSA-driven enhancement factor R (Eq. 6) under varying concentrations of MSA, HIO_3, and HIO_2 (i.e., [MSA], [HIO_3], and [HIO_2], units: molec. cm^{-3}).

$$R = \frac{J(\mathrm{HIO_3{-}HIO_2{-}MSA})}{J(\mathrm{HIO_3{-}HIO_2})} = \frac{J([\mathrm{HIO_3}]=x,[\mathrm{HIO_2}]=y,[\mathrm{MSA}]=z)}{J([\mathrm{HIO_3}]=x,[\mathrm{HIO_2}]=y)}, \quad (6)$$

where J(HIO_3–HIO_2–MSA) and J(HIO_3–HIO_2) represent the cluster formation rate of the HIO_3–HIO_2–MSA and HIO_3–HIO_2 system, respectively. x, y, and z are the adopted [HIO_3], [HIO_2], and [MSA], respectively.

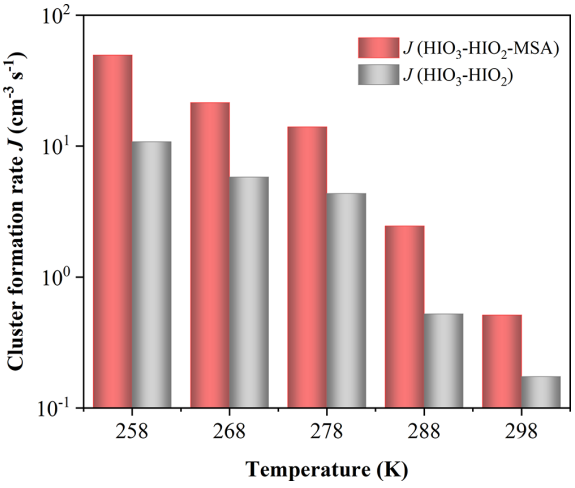

Figure 4. Simulated cluster formation rates J ($cm^{-3}\ s^{-1}$) against varying atmospheric temperatures: T = 258–298 K, CS = $2.0\times10^{-3}\ s^{-1}$, [HIO_3] = 1.0×10^7, [HIO_2] = 2.0×10^5, and [MSA] = 1.0×10^7 molec. cm^{-3}.

As seen from Fig. 5, with [MSA] ranging from 10^6 to 10^8 molec. cm^{-3} (Fig. 5a–c), the maximum R increases 5- to 10^4-fold, which is primarily due to MSA-mediated synergistic nucleation with HIO_3 and HIO_2 (recalling Sect. 3.2). Even at a median [MSA] of 1.0×10^7 molec. cm^{-3}, the resulting R can increase approximately 10^2-fold. In contrast, R is decayed under conditions of higher [HIO_3] and [HIO_2]. Furthermore, under the conditions with lower [HIO_3]/[HIO_2], where R is higher, the contribution of MSA nucleating with HIO_2 increases due to the relative scarcity of HIO_3. Conversely, R decreases at higher [HIO_3]/[HIO_2]; i.e., the impacts of MSA decrease. That is, the enhancing effect of MSA on J is limited in near-iodine source regions. Naturally, in regions with sparser iodine, the promoting effect of MSA is significant. However, the atmospheric [HIO_3] ranges widely from 10^6 to 10^8 molec. cm^{-3}. When [HIO_3] is comparable to or higher than [MSA], the HIO_3–HIO_2 pathway contributes more, and the R of MSA decreases with the rising [HIO_3]. It is worth noting that when [HIO_3] is comparable to [MSA], the R of MSA is greater than 2, as the contribution of MSA to clustering includes not only the direct formation of HIO_3–HIO_2–MSA clusters (∼ 20 %), but also its "catalysis" role in facilitating the formation of initial HIO_3–HIO_2 clusters (Fig. S7). To sum up, MSA can promote nucleation, particularly in marine regions characterized by lower T and lower [HIO_3] and [HIO_2]. In addition, we also considered the conditions in relatively polluted (CS = $1.0\times10^{-2}\ s^{-1}$) and clean (CS = $1.0\times10^{-4}\ s^{-1}$) environments and found that, similarly to the environment with a CS value of $2.0\times10^{-3}\ s^{-1}$, MSA exhibits a significant promoting effect on iodine particle formation (Figs. S8–S11). Furthermore, the effect of HIO_2 addition on the whole nucleation system was considered, as it is not only a rate-limiting step for cluster formation, leading

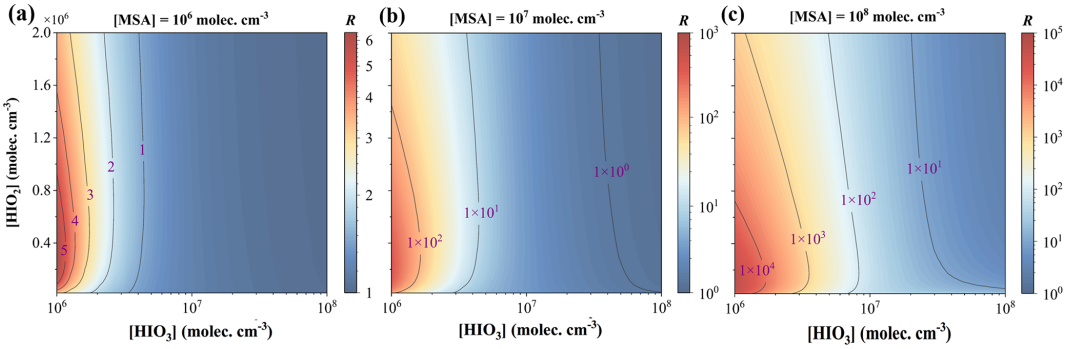

Figure 5. Enhancement strength R of MSA acting on cluster formation rates at varying precursor concentrations: $[HIO_3] = 10^6$–10^8 and $[HIO_2] = 2.0 \times 10^4$–$2.0 \times 10^6$ molec. cm^{-3} for **(a)** $[MSA] = 1.0 \times 10^6$ molec. cm^{-3}, **(b)** $[MSA] = 1.0 \times 10^7$ molec. cm^{-3}, and **(c)** $[MSA] = 1.0 \times 10^8$ molec. cm^{-3}; $T = 278$ K and $CS = 2.0 \times 10^{-3}$ s^{-1}.

to a significant increase in $J(HIO_3$–HIO_2–MSA) compared to $J(HIO_3$–MSA) (Fig. S12), but also thermodynamically favorable due to the HIO_3–HIO_2–MSA path being almost barrierless (1.24 kcal mol^{-1}) compared to the HIO_3–MSA pathway (Fig. S13).

3.4 Comparison with field observations

To further assess the atmospheric implications of the proposed HIO_3–HIO_2–MSA nucleation, we simulated J, shown in Fig. 6, based on the ambient conditions of the typical polar regions (e.g., Ny-Ålesund and Marambio) and the mid-latitude marine regions (e.g., Mace Head and Réunion). Subsequently, we compared these simulation results with observed nucleation rates, and the definition of the cluster formation rate is detailed in the Supplement. As shown in Fig. 6a, the $J(HIO_3$–HIO_2–MSA) simulated at $T = 268$ K, $CS = 4.0 \times 10^{-4}$ s^{-1}, $[HIO_3] = 10^5$–10^6, $[HIO_2] = 2.0 \times 10^3$–$2.0 \times 10^4$, and $[MSA] = 10^6$–10^8 molec. cm^{-3} was compared with field observations in coastal Ny-Ålesund (Beck et al., 2021; He et al., 2021). Both $J(HIO_3$–HIO_2–MSA) and $J(HIO_3$–$HIO_2)$ increase with the rising $[HIO_3]$ and $[HIO_2]$. Importantly, the addition of MSA effectively promotes J to a higher level (orange area), aligning with most field measurements (1.2×10^{-3}–1.2×10^{-1} cm^{-3} s^{-1}, gray lines) (Beck et al., 2021). Even when [MSA] is as low as 1.0×10^6 molec. cm^{-3} (the orange line below), the $J(HIO_3$–HIO_2–MSA) can be 1 order of magnitude higher than the observed J of 1.2×10^{-3} cm^{-3} s^{-1} (the gray line below). Moreover, the simulated J in Fig. 6b was obtained under the conditions of coastal Marambio, Antarctica: $T = 273$ K, $CS = 1.0 \times 10^{-4}$ s^{-1}, $[HIO_3] = 10^5$–10^6, $[HIO_2] = 2.0 \times 10^3$–$2.0 \times 10^4$, and $[MSA] = 10^6$–10^7 molec. cm^{-3} (Quéléver et al., 2022; He et al., 2021). Compared to $J(HIO_3$–$HIO_2)$, the MSA-enhanced $J(HIO_3$–HIO_2–MSA) is overall higher, better fitting with the field observations (1.2×10^{-1}–2.4×10^1 cm^{-3} s^{-1}, gray line) (Quéléver et al., 2022). These findings imply that MSA potentially plays a vital role in cold polar oceanic regions, particularly with higher [MSA] during NPF events.

In addition, the influence of HIO_3–HIO_2–MSA nucleation over the relatively warmer mid-latitude marine areas, such as Mace Head and Réunion, was investigated here (Fig. S14). We found that $J(HIO_3$–HIO_2–MSA) is slightly higher than $J(HIO_3$–$HIO_2)$, especially in regions with high concentrations of iodine oxoacids (e.g., Mace Head), showing a relatively limited enhancement effect of MSA on nucleation. Based on the simulated $J(HIO_3$–$HIO_2)$ ($\sim 1.2 \times 10^4$ cm^{-3} s^{-1}), iodine nucleation can almost completely explain the NPF events of Mace Head (Fig. S14a), which provides potential theoretical evidence for explaining the previous findings (Sipilä et al., 2016).

Overall, in the mid-latitude oceans, especially near iodine sources like Mace Head, MSA may have a limited enhancement effect on nucleation. In this case, the clustering process is dominated by abundant iodine oxoacids, while in the colder polar regions, particularly those with higher [MSA] like Marambio, MSA indeed significantly facilitates HIO_3–HIO_2 nucleation, suggesting a vital role in polar NPF.

4 Conclusion

The present study systematically investigates the HIO_3–HIO_2-based nucleation process enhanced by MSA at the molecular level by QC calculations and ACDC simulations. The results indicate that MSA can stabilize HIO_3–HIO_2-based clusters by building the intricate networks with more HBs and XBs. During clustering, MSA replaces HIO_3 in protonating HIO_2 to form ion pairs, resulting in relatively strong electrostatic attractions. In addition, thermodynamic analyses suggest that MSA-involved clustering is nearly barrierless. Compared to the HIO_3–HIO_2 system reported previously, the MSA-involved synergistic nucleation with HIO_3 and HIO_2 proceeds more efficiently, through two additional clustering pathways: (i) HIO_2–MSA binary and (ii) HIO_3–HIO_2–MSA ternary pathways. Moreover, the resulting en-

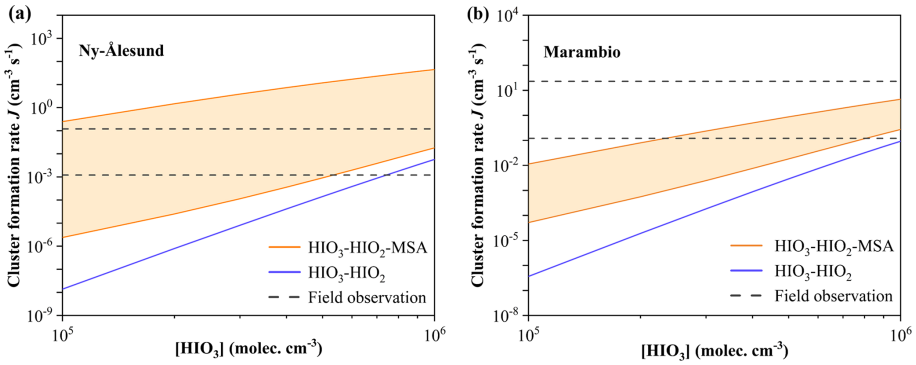

Figure 6. Comparison with the simulated cluster formation rates (J, $cm^{-3}\ s^{-1}$) and field observations under the ambient conditions of **(a)** Ny-Ålesund ($T = 268$ K; CS $= 4.0 \times 10^{-4}\ s^{-1}$; and $[HIO_3] = 10^5$–10^6, $[HIO_2] = 2.0 \times 10^3$–$2.0 \times 10^4$, and $[MSA] = 10^6$–10^8 molec. cm^{-3}) and **(b)** Marambio ($T = 273$ K; CS $= 1.0 \times 10^{-4}\ s^{-1}$; and $[HIO_3] = 10^5$–10^6, $[HIO_2] = 2.0 \times 10^3$–$2.0 \times 10^4$, and $[MSA] = 10^6$–10^7 molec. cm^{-3}). The orange area, blue line, and gray line represent $J(HIO_3$–HIO_2–MSA), $J(HIO_3$–$HIO_2)$, and J(field observation), respectively. $[HIO_3]/[HIO_2]$ is a constant.

hancement effect of MSA on nucleation is more substantial in colder regions, especially with richer MSA, but weaker in the environments near iodine sources. Further comparison with field observations indicates that HIO_3–HIO_2–MSA synergistic nucleation plays a limited role in mid-latitude ocean regions, particularly in regions with abundant iodine (e.g., Mace Head), but a potential role in colder polar regions (e.g., Ny-Ålesund and Marambio).

This study highlights the essential enhancing role of MSA in iodine oxoacids nucleation, and the HIO_3–HIO_2–MSA synergistic nucleation may help to explain the observation of abundant iodine particles during marine NPF events. Given the complex oceanic atmosphere, other potential nucleation precursors beyond MSA, such as sulfuric acid and amines, may also affect the HIO_3–HIO_2 nucleation process and further contribute to the formation of marine iodine particles, deserving future investigations.

Data availability. The data in this article are available from the corresponding authors upon request (anning@bit.edu.cn and zhangxiuhui@bit.edu.cn).

Supplement. The supplement related to this article is available online at: https://doi.org/10.5194/acp-24-3989-2024-supplement.

Author contributions. XZ designed and supervised the research. JL and NW performed the quantum chemical calculations and the ACDC simulations. JL, NW, BC, and AN analyzed data. JL, AN, and XZ wrote the paper with contributions from all of the other coauthors.

Competing interests. The contact author has declared that none of the authors has any competing interests.

Disclaimer. Publisher's note: Copernicus Publications remains neutral with regard to jurisdictional claims made in the text, published maps, institutional affiliations, or any other geographical representation in this paper. While Copernicus Publications makes every effort to include appropriate place names, the final responsibility lies with the authors.

Acknowledgements. We acknowledge the National Supercomputing Center in Shenzhen for providing the computational resources and the TURBOMOLE program.

Financial support. This research has been supported by the National Science Fund for Distinguished Young Scholars (grant no. 22225607), the National Natural Science Foundation of China (grant nos. 22306011, 42105101, 22376013, 22122610, and 21976015), and the Beijing Institute of Technology Science and Technology Innovation Program (grant no. 2021CX01010). An Ning was supported by the China Postdoctoral Science Foundation (grant no. 2023M730236).

Review statement. This paper was edited by Zhibin Wang and reviewed by four anonymous referees.

References

Ahlrichs, R., Bär, M., Häser, M., Horn, H., and Kölmel, C.: Electronic structure calculations on workstation computers: The program system turbomole, Chem. Phys. Lett., 162, 165–169, https://doi.org/10.1016/0009-2614(89)85118-8, 1989.

Almeida, J., Schobesberger, S., Kürten, A., Ortega, I. K., Kupiainen-Määttä, O., Praplan, A. P., Adamov, A., Amorim, A., Bianchi, F., Breitenlechner, M., David, A., Dommen, J., Donahue, N. M., Downard, A., Dunne, E., Duplissy, J., Ehrhart, S., Flagan, R. C., Franchin, A., Guida, R., Hakala, J., Hansel, A., Heinritzi, M., Henschel, H., Jokinen, T., Junninen, H., Kajos, M.,

Kangasluoma, J., Keskinen, H., Kupc, A., Kurten, T., Kvashin, A. N., Laaksonen, A., Lehtipalo, K., Leiminger, M., Leppä, J., Loukonen, V., Makhmutov, V., Mathot, S., McGrath, M. J., Nieminen, T., Olenius, T., Onnela, A., Petäjä, T., Riccobono, F., Riipinen, I., Rissanen, M., Rondo, L., Ruuskanen, T., Santos, F. D., Sarnela, N., Schallhart, S., Schnitzhofer, R., Seinfeld, J. H., Simon, M., Sipilä, M., Stozhkov, Y., Stratmann, F., Tomé, A., Tröstl, J., Tsagkogeorgas, G., Vaattovaara, P., Viisanen, Y., Virtanen, A., Vrtala, A., Wagner, P. E., Weingartner, E., Wex, H., Williamson, C., Wimmer, D., Ye, P., Yli-Juuti, T., Carslaw, K. S., Kulmala, M., Curtius, J., Baltensperger, U., Worsnop, D. R., Vehkamäki, H., and Kirkby, J.: Molecular understanding of sulphuric acid-amine particle nucleation in the atmosphere, Nature, 502, 359–363, https://doi.org/10.1038/nature12663, 2013.

Baccarini, A., Karlsson, L., Dommen, J., Duplessis, P., Vullers, J., Brooks, I. M., Saiz-Lopez, A., Salter, M., Tjernstrom, M., Baltensperger, U., Zieger, P., and Schmale, J.: Frequent new particle formation over the high Arctic pack ice by enhanced iodine emissions, Nat. Commun., 11, 4924, https://doi.org/10.1038/s41467-020-18551-0, 2020.

Beck, L. J., Sarnela, N., Junninen, H., Hoppe, C. J. M., Garmash, O., Bianchi, F., Riva, M., Rose, C., Peräkylä, O., Wimmer, D., Kausiala, O., Jokinen, T., Ahonen, L., Mikkilä, J., Hakala, J., He, X. C., Kontkanen, J., Wolf, K. K. E., Cappelletti, D., Mazzola, M., Traversi, R., Petroselli, C., Viola, A. P., Vitale, V., Lange, R., Massling, A., Nøjgaard, J. K., Krejci, R., Karlsson, L., Zieger, P., Jang, S., Lee, K., Vakkari, V., Lampilahti, J., Thakur, R. C., Leino, K., Kangasluoma, J., Duplissy, E. M., Siivola, E., Marbouti, M., Tham, Y. J., Saiz-Lopez, A., Petäjä, T., Ehn, M., Worsnop, D. R., Skov, H., Kulmala, M., Kerminen, V. M., and Sipilä, M.: Differing Mechanisms of New Particle Formation at Two Arctic Sites, Geophys. Res. Lett., 48, e2020GL091334, https://doi.org/10.1029/2020gl091334, 2021.

Berresheim, H., Elste, T., Rosman, K., Dal Maso, M., Tremmel, H. G., Mäkelä, J. M., Allen, A. G., Kulmala, M., and Hansson, H.-C.: Gas-aerosol relationships of H_2SO_4, MSA, and OH: Observations in the coastal marine boundary layer at Mace Head, Ireland, J. Geophys. Res.-Atmos., 107, PAR 5-1–PAR 5-12, https://doi.org/10.1029/2000jd000229, 2002.

Bork, N., Elm, J., Olenius, T., and Vehkamäki, H.: Methane sulfonic acid-enhanced formation of molecular clusters of sulfuric acid and dimethyl amine, Atmos. Chem. Phys., 14, 12023–12030, https://doi.org/10.5194/acp-14-12023-2014, 2014.

Brean, J., Dall'Osto, M., Simó, R., Shi, Z., Beddows, D. C. S., and Harrison, R. M.: Open ocean and coastal new particle formation from sulfuric acid and amines around the Antarctic Peninsula, Nat. Geosci., 14, 383–388, https://doi.org/10.1038/s41561-021-00751-y, 2021.

Chen, L., Wang, J., Gao, Y., Xu, G., Yang, X., Lin, Q., and Zhang, Y.: Latitudinal distributions of atmospheric MSA and MSA/nss-SO_4^{2-} ratios in summer over the high latitude regions of the Southern and Northern Hemispheres, J. Geophys. Res.-Atmos., 117, D10306, https://doi.org/10.1029/2011JD016559, 2012.

Chen, Q., Sherwen, T., Evans, M., and Alexander, B.: DMS oxidation and sulfur aerosol formation in the marine troposphere: a focus on reactive halogen and multiphase chemistry, Atmos. Chem. Phys., 18, 13617–13637, https://doi.org/10.5194/acp-18-13617-2018, 2018.

Dal Maso, M., Kulmala, M., Lehtinen, K. E. J., Mäkelä, J. M., Aalto, P., and O'Dowd, C. D.: Condensation and coagulation sinks and formation of nucleation mode particles in coastal and boreal forest boundary layers, J. Geophys. Res.-Atmos., 107, PAR 2-1–PAR 2-10, https://doi.org/10.1029/2001jd001053, 2002.

Eisele, F. L. and Tanner, D. J.: Measurement of the gas phase concentration of H_2SO_4 and methane sulfonic acid and estimates of H_2SO_4 production and loss in the atmosphere, J. Geophys. Res., 98, 9001–9010, https://doi.org/10.1029/93JD00031, 1993.

Francl, M. M., Pietro, W. J., Hehre, W. J., Binkley, J. S., Gordon, M. S., DeFrees, D. J., and Pople, J. A.: Self-consistent molecular orbital methods. XXIII. A polarization-type basis set for second-row elements, J. Chem. Phys., 77, 3654–3665, https://doi.org/10.1063/1.444267, 1982.

Frisch, M. J., Trucks, G. W., Schlegel, H. B., Scuseria, G. E., Robb, M. A., Cheeseman, J. R., Scalmani, G., Barone, V., Mennucci, B., Petersson, G. A., Nakatsuji, H., Caricato, M., Li, X., Hratchian, H. P., Izmaylov, A. F., Bloino, J., Zheng, G., Sonnenberg, J. L., Hada, M., Ehara, M., Toyota, K., Fukuda, R., Hasegawa, J., Ishida, M., Nakajima, T., Honda, Y., Kitao, O., Nakai, H., Vreven, T., Montgomery, J. A., Peralta, J. E., Ogliaro, F., Bearpark, M., Heyd, J. J., Brothers, E., Kudin, K. N., Staroverov, V. N., Kobayashi, R., Normand, J., Raghavachari, K., Rendell, A., Burant, J. C., Iyengar, S. S., Tomasi, J., Cossi, M., Rega, N., Millam, J. M., Klene, M., Knox, J. E., Cross, J. B., Bakken, V., Adamo, C., Jaramillo, J., Gomperts, R., Stratmann, R. E., Yazyev, O., Austin, A. J., Cammi, R., Pomelli, C., Ochterski, J. W., Martin, R. L., Morokuma, K., Zakrzewski, V. G., Voth, G. A., Salvador, P., Dannenberg, J. J., Dapprich, S., Daniels, A. D., Farkas, O., Foresman, J. B., Ortiz, J. V., Cioslowski, J., and Fox, D. J.: Gaussian 09, Revision A.02, Gaussian Inc, Wallingford CT, https://gaussian.com/g09citation/ (last access: 7 May 2022), 2009.

Grabowski, S. J.: Hydrogen bonding strength – measures based on geometric and topological parameters, J. Phys. Org. Chem., 17, 18–31, https://doi.org/10.1002/poc.685, 2004.

Hättig, C. and Weigend, F.: CC2 excitation energy calculations on large molecules using the resolution of the identity approximation, J. Chem. Phys., 113, 5154–5161, https://doi.org/10.1063/1.1290013, 2000.

He, X.-C., Tham, Y. J., Dada, L., Wang, M., Finkenzeller, H., Stolzenburg, D., Iyer, S., Simon, M., Kürten, A. K., Shen, J., Roerup, B., Rissanen, M., Schobesberger, S., Baalbaki, R., Wang, D. S., Koenig, T. K., Jokinen, T., Sarnela, N., Beck, L. J., Almeida, J., Amanatidis, S., Amorim, A., Ataei, F., Baccarini, A., Bertozzi, B., Bianchi, F., Brilke, S., Caudillo, L., Chen, D., Chiu, R., Chu, B., Dias, A., Ding, A., Dommen, J., Duplissy, J., Haddad, I. E., Carracedo, L. G., Granzin, M., Hansel, A., Heinritzi, M., Hofbauer, V., Junninen, H., Kangasluoma, J., Kemppainen, D., Kim, C., Kong, W., Krechmer, J. E., Kvashin, A., Laitinen, T., Lamkaddam, H., Lee, C. P., Lehtipalo, K., Leiminger, M., Li, Z., Makhmutov, V., Manninen, H. E., Marie, G., Marten, R., Mathot, S., Mauldin, R. L., Mentler, B., Moehler, O., Mueller, T., Nie, W., Onnela, A., Petaja, T., Pfeifer, J., Philippov, M., Ranjithkumar, A., Saiz-Lopez, A., Salma, I., Scholz, W., Schuchmann, S., Schulze, B., Steiner, G., Stozhkov, Y., Tauber, C., Tome, A., Thakur, R. C., Vaisanen, O., Vazquez-Pufleau, M., Wagner, A. C., Wang, Y., Weber, S. K., Winkler, P. M., Wu,

Y., Xiao, M., Yan, C., Ye, Q., Ylisirnio, A., Zauner-Wieczorek, M., Zha, Q., Zhou, P., Flagan, R. C., Curtius, J., Baltensperger, U., Kulmala, M., Kerminen, V.-M., Kurten, T., Donahue, N. M., Volkamer, R., Kirkby, J., Worsnop, D. R., and Sipila, M.: Role of iodine oxoacids in atmospheric aerosol nucleation, Science, 371, 589–595, https://doi.org/10.1126/science.abe0298, 2021.

Koch, U. and Popelier, P. L. A.: Characterization of C-H-O Hydrogen Bonds on the Basis of the Charge Density, J. Phys. Chem., 99, 9747–9754, https://doi.org/10.1021/j100024a016, 1995.

Kulmala, M., Kontkanen, J., Junninen, H., Lehtipalo, K., Manninen, H. E., Nieminen, T., Petäjä, T., Sipilä, M., Schobesberger, S., Rantala, P., Franchin, A., Jokinen, T., Järvinen, E., Äijälä, M., Kangasluoma, J., Hakala, J., Aalto, P. P., Paasonen, P., Mikkilä, J., Vanhanen, J., Aalto, J., Hakola, H., Makkonen, U., Ruuskanen, T., Mauldin, R. L., Duplissy, J., Vehkamäki, H., Bäck, J., Kortelainen, A., Riipinen, I., Kurtén, T., Johnston, M. V., Smith, J. N., Ehn, M., Mentel, T. F., Lehtinen, K. E., Laaksonen, A., Kerminen, V. M., and Worsnop, D. R.: Direct observations of atmospheric aerosol nucleation, Science, 339, 943–946, https://doi.org/10.1126/science.1227385, 2013.

Kürten, A., Li, C., Bianchi, F., Curtius, J., Dias, A., Donahue, N. M., Duplissy, J., Flagan, R. C., Hakala, J., Jokinen, T., Kirkby, J., Kulmala, M., Laaksonen, A., Lehtipalo, K., Makhmutov, V., Onnela, A., Rissanen, M. P., Simon, M., Sipilä, M., Stozhkov, Y., Tröstl, J., Ye, P., and McMurry, P. H.: New particle formation in the sulfuric acid–dimethylamine–water system: reevaluation of CLOUD chamber measurements and comparison to an aerosol nucleation and growth model, Atmos. Chem. Phys., 18, 845–863, https://doi.org/10.5194/acp-18-845-2018, 2018.

Lane, J. R., Contreras-García, J., Piquemal, J. P., Miller, B. J., and Kjaergaard, H. G.: Are Bond Critical Points Really Critical for Hydrogen Bonding?, J. Chem. Theory Comput., 9, 3263–3266, https://doi.org/10.1021/ct400420r, 2013.

Lee, S. H., Gordon, H., Yu, H., Lehtipalo, K., Haley, R., Li, Y., and Zhang, R.: New Particle Formation in the Atmosphere: From Molecular Clusters to Global Climate, J. Geophys. Res.-Atmos., 124, 7098–7146, https://doi.org/10.1029/2018jd029356, 2019.

Liu, L., Li, S., Zu, H., and Zhang, X.: Unexpectedly significant stabilizing mechanism of iodous acid on iodic acid nucleation under different atmospheric conditions, Sci. Total Environ., 859, 159832, https://doi.org/10.1016/j.scitotenv.2022.159832, 2023.

Liu, Y., Xie, H.-B., Ma, F., Chen, J., and Elm, J.: Amine-Enhanced Methanesulfonic Acid-Driven Nucleation: Predictive Model and Cluster Formation Mechanism, Environ. Sci. Technol., 56, 7751–7760, https://doi.org/10.1021/acs.est.2c01639, 2022.

Lu, T. and Chen, F.: Multiwfn: a multifunctional wavefunction analyzer, J. Comput. Chem., 33, 580–592, https://doi.org/10.1002/jcc.22885, 2012.

Lu, T. and Chen, Q.: Shermo: A general code for calculating molecular thermochemistry properties, Comput. Theor. Chem., 1200, 113249, https://doi.org/10.1016/j.comptc.2021.113249, 2021.

Lu, Y., Liu, L., Ning, A., Yang, G., Liu, Y., Kurtén, T., Vehkamäki, H., Zhang, X., and Wang, L.: Atmospheric Sulfuric Acid-Dimethylamine Nucleation Enhanced by Trifluoroacetic Acid, Geophys. Res. Lett., 47, e2019GL085627, https://doi.org/10.1029/2019gl085627, 2020.

Ma, F., Xie, H. B., Zhang, R., Su, L., Jiang, Q., Tang, W., Chen, J., Engsvang, M., Elm, J., and He, X. C.: Enhancement of Atmospheric Nucleation Precursors on Iodic Acid-Induced Nucleation: Predictive Model and Mechanism, Environ. Sci. Technol., 57, 6944–6954, https://doi.org/10.1021/acs.est.3c01034, 2023.

McGrath, M. J., Olenius, T., Ortega, I. K., Loukonen, V., Paasonen, P., Kurtén, T., Kulmala, M., and Vehkamäki, H.: Atmospheric Cluster Dynamics Code: a flexible method for solution of the birth-death equations, Atmos. Chem. Phys., 12, 2345–2355, https://doi.org/10.5194/acp-12-2345-2012, 2012.

Ning, A., Liu, L., Ji, L., and Zhang, X.: Molecular-level nucleation mechanism of iodic acid and methanesulfonic acid, Atmos. Chem. Phys., 22, 6103–6114, https://doi.org/10.5194/acp-22-6103-2022, 2022.

O'Dowd, C. D. and de Leeuw, G.: Marine aerosol production: a review of the current knowledge, Philos. T. R. Soc. A. 365, 1753–1774, https://doi.org/10.1098/rsta.2007.2043, 2007.

O'Dowd, C. D., Hämeri, K., Mäkelä, J. M., Pirjola, L., Kulmala, M., Jennings, S. G., Berresheim, H., Hansson, H.-C., Leeuw, G. d., Kunz, G. J., Allen, A. G., Hewitt, C. N., Jackson, A., Viisanen, Y., and Hoffmann, T.: A dedicated study of New Particle Formation and Fate in the Coastal Environment (PARFORCE): Overview of objectives and achievements, J. Geophys. Res.-Atmos., 107, PAR 1-1–PAR 1-16, https://doi.org/10.1029/2001jd000555, 2002.

Peterson, K. A., Figgen, D., Goll, E., Stoll, H., and Dolg, M.: Systematically convergent basis sets with relativistic pseudopotentials. II. Small-core pseudopotentials and correlation consistent basis sets for the post-d group 16–18 elements, J. Chem. Phys., 119, 11113–11123, https://doi.org/10.1063/1.1622924, 2003.

Pöschl, U.: Atmospheric aerosols: composition, transformation, climate and health effects, Angew. Chem. Int. Edit., 44, 7520–4750, https://doi.org/10.1002/anie.200501122, 2005.

Quéléver, L. L. J., Dada, L., Asmi, E., Lampilahti, J., Chan, T., Ferrara, J. E., Copes, G. E., Pérez-Fogwill, G., Barreira, L., Aurela, M., Worsnop, D. R., Jokinen, T., and Sipilä, M.: Investigation of new particle formation mechanisms and aerosol processes at Marambio Station, Antarctic Peninsula, Atmos. Chem. Phys., 22, 8417–8437, https://doi.org/10.5194/acp-22-8417-2022, 2022.

Read, K. A., Lewis, A. C., Bauguitte, S., Rankin, A. M., Salmon, R. A., Wolff, E. W., Saiz-Lopez, A., Bloss, W. J., Heard, D. E., Lee, J. D., and Plane, J. M. C.: DMS and MSA measurements in the Antarctic Boundary Layer: impact of BrO on MSA production, Atmos. Chem. Phys., 8, 2985–2997, https://doi.org/10.5194/acp-8-2985-2008, 2008.

Rong, H., Liu, J., Zhang, Y., Du, L., Zhang, X., and Li, Z.: Nucleation mechanisms of iodic acid in clean and polluted coastal regions, Chemosphere, 253, 126743, https://doi.org/10.1016/j.chemosphere.2020.126743, 2020.

Saltzman, E. S., Savoie, D. L., Zika, R. G., and Prospero, J. M.: Methane sulfonic acid in the marine atmosphere, J. Geophys. Res., 88, 10897–10902, https://doi.org/10.1029/JC088iC15p10897, 1983.

Shen, J., Xie, H.-B., Elm, J., Ma, F., Chen, J., and Vehkamäki, H.: Methanesulfonic Acid-driven New Particle Formation Enhanced by Monoethanolamine: A Computational Study, Environ. Sci. Technol., 53, 14387–14397, https://doi.org/10.1021/acs.est.9b05306, 2019.

Shen, J., Elm, J., Xie, H.-B., Chen, J., Niu, J., and Vehkamäki, H.: Structural Effects of Amines in Enhancing Methanesulfonic Acid-Driven New Particle Formation, Environ. Sci. Technol., 54, 13498–13508, https://doi.org/10.1021/acs.est.0c05358, 2020.

Sipilä, M., Sarnela, N., Jokinen, T., Henschel, H., Junninen, H., Kontkanen, J., Richters, S., Kangasluoma, J., Franchin, A., peräkylä, O., Rissanen, M. P., Ehn, M., Vehkamäki, H., Kurten, T., Berndt, T., Petäjä, T., Worsnop, D., Ceburnis, D., Kerminen, V. M., Kulmala, M., and O'Dowd, C.: Molecular-scale evidence of aerosol particle formation via sequential addition of HIO_3, Nature, 537, 532–534, https://doi.org/10.1038/nature19314, 2016.

Vehkamäki, H.: Classical Nucleation Theory in Multicomponent Systems, Springer Science & Business Media, https://doi.org/10.1007/1003-1540-31218-31218, 2006.

Wang, L., Khalizov, A. F., Zheng, J., Xu, W., Ma, Y., Lal, V., and Zhang, R.: Atmospheric nanoparticles formed from heterogeneous reactions of organics, Nat. Geosci., 3, 238–242, https://doi.org/10.1038/ngeo778, 2010.

Wu, N., Ning, A., Liu, L., Zu, H., Liang, D., and Zhang, X.: Methanesulfonic acid and iodous acid nucleation: a novel mechanism for marine aerosols, Phys. Chem. Chem. Phys., 25, 16745–16752, https://doi.org/10.1039/d3cp01198d, 2023.

Yan, J., Jung, J., Zhang, M., Xu, S., Lin, Q., Zhao, S., and Chen, L.: Significant Underestimation of Gaseous Methanesulfonic Acid (MSA) over Southern Ocean, Environ. Sci. Technol., 53, 13064–13070, https://doi.org/10.1021/acs.est.9b05362, 2019.

Yu, H., Ren, L., Huang, X., Xie, M., He, J., and Xiao, H.: Iodine speciation and size distribution in ambient aerosols at a coastal new particle formation hotspot in China, Atmos. Chem. Phys., 19, 4025–4039, https://doi.org/10.5194/acp-19-4025-2019, 2019.

Zhang, R.: Getting to the Critical Nucleus of Aerosol Formation, Science, 328, 1366–1367, https://doi.org/10.1126/science.1189732, 2010.

Zhang, R., Khalizov, A., Wang, L., Hu, M., and Xu, W.: Nucleation and growth of nanoparticles in the atmosphere, Chem. Rev., 112, 1957–2011, https://doi.org/10.1021/cr2001756, 2012.

Zhang, R., Xie, H. B., Ma, F., Chen, J., Iyer, S., Simon, M., Heinritzi, M., Shen, J., Tham, Y. J., Kurtén, T., Worsnop, D. R., Kirkby, J., Curtius, J., Sipilä, M., Kulmala, M., and He, X. C.: Critical Role of Iodous Acid in Neutral Iodine Oxoacid Nucleation, Environ. Sci. Technol., 56, 14166–14177, https://doi.org/10.1021/acs.est.2c04328, 2022.

Zhang, S., Li, S., Ning, A., Liu, L., and Zhang, X.: Iodous acid – a more efficient nucleation precursor than iodic acid, Phys. Chem. Chem. Phys., 24, 13651–13660, https://doi.org/10.1039/d2cp00302c, 2022.